GEOPHYSICS, VOL. 68, NO. 4 (JULY-AUGUST 2003); P. 1389–1398, 11 FIGS., 1 TABLE.
10.1190/1.1598132

White's model for wave propagation in partially saturated rocks: Comparison with poroelastic numerical experiments

José M. Carcione*, Hans B. Helle‡, and Nam H. Pham**

ABSTRACT

We use a poroelastic modeling algorithm to compute numerical experiments of wave propagation in White's partial saturation model. The results are then compared to the theoretical predictions. The model consists of a homogeneous sandstone saturated with brine and spherical gas pockets. White's theory predicts a relaxation mechanism, due to pressure equilibration, causing attenuation and velocity dispersion of the wavefield. We vary gas saturation either by increasing the radius of the gas pocket or by increasing the density of gas bubbles. Despite that the modeling is two dimensional and interaction between the gas pockets is neglected in White's model, the numerical results show the trends predicted by the theory. In particular, we observe a similar increase in velocity at high frequencies (and low permeabilities). Furthermore, the behavior of the attenuation peaks versus water saturation and frequency is similar to that of White's model. The modeling results show more dissipation and higher velocities than White's model due to multiple scattering and local fluid-flow effects. The conversion of fast P-wave energy into dissipating slow waves at the patches is the main mechanism of attenuation. Differential motion between the rock skeleton and the fluids is highly enhanced by the presence of fluid/fluid interfaces and pressure gradients generated through them.

INTRODUCTION

Microstructural properties of reservoir rocks and their in-situ rock conditions can be obtained, in principle, from seismic properties, such as traveltimes, amplitude information, and wave polarization. In particular, although it is known from the early 1980s that the dominating mechanisms of wave attenuation are oscillating flow of the viscous pore fluids and grain boundary friction (e.g., Winkler and Nur, 1982), the use of attenuation to characterize the rock properties is still underexploited.

Regions of nonuniform patchy saturation occur at gas-oil and gas-water contacts in hydrocarbon reservoirs. Also, during production, gas may come out of solution and create pockets of free gas. When laboratory measurements and sonic logs are used to infer the behavior of acoustic properties at seismic frequencies, the frequency dependence of these properties becomes a key factor. As demonstrated by White (1975), wave velocity and attenuation are substantially affected by the presence of partial (patchy) saturation, mainly depending on the size of the gas pockets (saturation), frequency, permeability, and porosity of rocks.

Patchy saturation effects on acoustic properties were observed by Murphy (1984) and Knight and Nolen-Hoecksema (1990). Cadoret et al. (1995) observed the phenomenon in the laboratory at the frequency range 1–500 kHz. Two different saturation methods result in different fluid distributions and produce two different values of velocity for the same saturation. Imbibition by depressurization produces a very homogeneous saturation, whereas drainage by drying produces heterogeneous saturations at high water saturation levels. In the latter case, the experiments show considerably higher velocities, as predicted by White's theory. The experimental results of Yin et al. (1992) display consistent peaks in resonance attenuation at high water saturation. A strong dependence on the saturation history is evident, with the attenuation peak located at 90% water saturation in the drainage experiment and at 98% water saturation for imbibition techniques.

White's model describes wave velocity and attenuation as a function of frequency, permeability, and porosity, among other parameters. Attenuation and velocity dispersion is caused by fluid flow between the water phase and the gas pockets, which have different pore pressures. The critical fluid diffusion relaxation scale is proportional to the square root of the ratio

Manuscript received by the Editor February 15, 2002; revised manuscript received October 7, 2002.
*Istituto Nazionale di Oceanografia e di Geofisica Sperimentale (OGS), Borgo Grotta Gigante 42c, 34010 Sgonico, Trieste, Italy E-mail: jcarcione@ogs.trieste.it.
‡Norsk Hydro a.s., E & P Research Centre, N-5020 Bergen, Norway. E-mail: hans.b.helle@nho.hydro.com.
**Norwegian University of Science and Technology, Department of Petroleum Engineering and Applied Geophysics, N-7491 Trondheim, Norway. E-mail: namhp@ipt.ntnu.no.

permeability to frequency (e.g., Mavko et al., 1998, 207). At seismic frequencies, the length scale is very large, and the pressure is nearly uniform throughout the medium, but as frequency increases, pore pressure differences can cause an important increase in P-wave velocity.

White's model considers spherical gas pockets located at the center of a cubic array saturated with liquid. For simplicity in the calculations, White considers two concentric spheres, where the volume of the outer sphere is the same as the volume of the elementary cube. The theory provides an average of the bulk modulus for a single gas pocket, without taking into account the interactions between gas pockets. Dutta and Odé (1979) rederived White's model using Biot's theory. Dutta and Seriff (1979) pointed out some corrections in White's equation, regarding the use of the P-wave modulus instead of the bulk modulus (see also Mavko et al., 1998, 208). Gist (1994) successfully used White's model to fit ultrasonic velocities obtained from saturations established using drainage techniques. He used saturation-dependent moduli as input to White's model instead of the dry-rock moduli. The predicted velocities, considering local fluid flow, are higher than the velocities predicted by White's model. Recently, Johnson (2001) developed a generalization of White's model for patches of arbitrary shape. This model has two geometrical parameters besides the usual parameters of Biot's theory: the specific surface area and the size of the patches.

Use of numerical simulations, based on the full-wave solution of the poroelastic equations, can be useful to study the physics of wave propagation in partially saturated rocks. Although White's model is an ideal representation of patchy saturation, its predictions are qualitatively correct, and the model serves as a reference theoretical framework. In this sense, it is useful to compare the results of White's model to numerical simulations based on Biot's theory of poroelasticity. We should, however, consider that the theory and the modeling code are based on the same theoretical basis (Biot's theory, although White's model does not take into account the interaction between gas pockets). This investigation can be the basis for more realistic analyses, where an arbitrary (general) pore-scale fluid distribution is considered. By using computerized tomography (CT) scans, it is possible to visualize the fluid distribution in real rocks (Cadoret et al., 1995). Fractal models, such as the von Kármán autocovariance function, calibrated by the CT scans, can be used to model realistic fluid distributions.

P-wave and S-wave velocities can be higher in partially saturated rocks than in dry rocks, but in some cases they are lower. As predicted by White's model, this behavior depends on frequency, viscosity, and permeability. It is therefore important to investigate the sensitivity and properties of wave velocity and attenuation versus pore-fluid distribution. This is the basis for direct hydrocarbon detection and enhanced oil recovery and monitoring, since techniques such as "bright spot" and amplitude variation with offset (AVO) analyses make use of those physical properties. The modeling methodology used in the present study constitutes a powerful computational tool to investigate the physics of wave propagation in porous rocks and, in some cases, can be used as an alternative method to laboratory experiments.

We solve the poroelastic equations with an algorithm developed by Carcione and Helle (1999), which uses a fourth-order Runge-Kutta time-stepping scheme and the staggered Fourier method for computing the spatial derivatives. The stiff part of the differential equations is solved with a time-splitting technique, which preserves the physics of the slow quasi-static wave at low frequencies.

PHASE VELOCITY AND ATTENUATION

The concept of complex velocity can be used to obtain the phase velocity and attenuation factor (e.g., Carcione, 2001, 55). Let v_c be the P-wave complex velocity obtained with White's model (see Appendix). Then, the phase velocity and attenuation factor are given by

$$c = \left[\mathrm{Re}\left(\frac{1}{v_c}\right)\right]^{-1} \tag{1}$$

and

$$\alpha = -\omega \mathrm{Im}\left(\frac{1}{v_c}\right), \tag{2}$$

respectively, where ω is the angular frequency. If we approximate the porous medium by a viscoelastic solid, the quality factor can be expressed as

$$Q = \frac{\mathrm{Re}(v_c^2)}{\mathrm{Im}(v_c^2)}. \tag{3}$$

[Otherwise, the Q factor for porous media has a more complex expression (Carcione, 2001, 289).]. The relation between the attenuation factor and the quality factor Q can be expressed as

$$\alpha = \frac{2\pi f}{c}\left(\sqrt{Q^2+1} - Q\right) \approx \frac{\pi f}{cQ}, \tag{4}$$

where $f = \omega/(2\pi)$ is the frequency (Carcione, 2001, 139). The second relation in the right side holds for low-loss solid ($Q \gg 1$).

The phase velocity in the numerical experiments is computed from the center of gravity of $|\mathbf{v}|^2$ versus propagation time, where $\mathbf{v}$ is the bulk particle-velocity field (Carcione, 1996). A set of receivers R_1 and R_3 located on five radial lines are used for the calculations, and receivers R_2 are used for verification. The numerical phase velocity is estimated by averaging the velocities obtained at the five receivers R_3. More details about this calculation are given in Carcione et al. (1996) and Carcione (2001, 145). The determination of phase velocity in terms of the location of the energy is justified from the fact that for isotropic media and homogeneous viscoelastic waves, the phase velocity is equal to the energy velocity (Carcione, 2001, 99).

To estimate attenuation, we use the classical spectral ratio approach discussed by Toksöz et al. (1979), implying that the amplitude ratio A_1/A_3 at the dominant frequency f satisfies

$$\ln\left[\frac{A_1(f, r_1)}{A_3(f, r_3)}\right] = \alpha(r_3 - r_1) + \ln\left(\frac{G_1}{G_3}\right), \tag{5}$$

where r_i denotes the source-receiver radial distances, and G_i denotes the respective geometrical spreading factors. Using relation (4), equation (5) can be rewritten as

$$\ln\left[\frac{A_1(f, r_1)}{A_3(f, r_3)}\right] = \frac{\pi f(r_3 - r_1)}{Qc} + \ln\left(\frac{G_1}{G_3}\right), \tag{6}$$

The quality factor is determined from the slope of the line fitted to $\ln(A_1/A_3)$.

A source of discrepancy between theory and numerical results can be due to the fact that White's model is three dimensional and the simulations are two dimensional. The travel time is not affected by the dimensionality of space (see, for instance, Carcione and Quiroga-Goode, 1996). Hence, the wave velocities are not affected. With regard to the amplitudes, equation (6) implicitly has the correction for geometrical spreading ($1/\sqrt{r}$ in 2D space and $1/r$ in 3D space). Therefore, the discrepancy could be solely due to the deviation of the 2D Green's function from the exponential function. The 2D and 3D Green's function for poroelastic media contain the kernels $H_0^{(2)}(x)$ and $\exp(ix)$, respectively, where $x=\omega r/c$, and $H_0^{(2)}$ is the Hankel function of the second kind (e.g., Carcione and Quiroga-Goode, 1996). The Hankel function approaches the exponential function for larges values of $|x|$. For instance, for $c=3000$ m/s, $r=0.05$ m, and $f=100$ kHz, the argument is $x=10.5$ The exact value of the Hankel function is $(-0.239, 0.061)$ and the asymptotic value is $(-0.238, 0.064)$. Even for $x=2$, the differences are not significant [$(0.22, -0.51)$ versus $(0.20, -0.53)$]. This fact indicates that the discrepancy due to the space dimension is not important.

RESULTS

We consider the material properties shown in Table 1, where the moduli and density of the grain material correspond to a mixture of 90% quartz and 10% clay [the moduli are calculated as the upper and lower Hashin-Shtrikman bounds (Mavko et al., 1998, 106)]. The dry-rock moduli are obtained by a relation introduced by Krief et al. (1990) (see Goldberg and Gurevich, 1998; and Carcione et al., 2000). Note that White's (1975) theory does not consider tortuosity [the value of tortuosity given in Table 1 is typical of a sandstone (e.g., Johnson et al., 1987)]. If a and b are the outer and inner radii of the gas pockets (see Appendix) and we denote the space dimension by n, water saturation can be expressed by $S_w=1-(a/b)^n$. A source of discrepancy between theoretical and numerical results may arise from the fact that White's theory does not consider the interaction between gas pockets, while this interaction is present in the numerical simulations.

The transition frequency separating the relaxed and unrelaxed states (that is, the location of the relaxation peak) is approximately given by

$$f_c=\frac{\kappa K_{E2}}{\pi\eta_2(b-a)^2}, \tag{7}$$

where κ is the permeability, K_{E2} is given in equation (A-6), and η_2 is the viscosity of water. Dutta and Seriff (1979) consider b^2, instead of $(b-a)^2$, in the denominator. However, the relevant relaxation distance should be the thickness of the outer shell (i.e., $b-a$). White considers a harmonic displacement applied to the outer spherical surface, which creates two different pressures in the outer shell and the inner sphere. Therefore, the relaxation distance should be the difference between the two radii (Gist, 1994). Relaxation frequencies of essentially the same physical nature, but for plane-layered rocks, have been given by White et al. (1975), Norris (1993), and Gurevich and Lopatnikov (1995).

There are two cases giving the same gas saturation. They are illustrated in Figure 1 for a 2D porous medium. Figure 1a shows four gas pockets, where the gas saturation is $S_g=4\pi a^2$ [the size of the square is $\ell=1/2$, and $b=\ell/\sqrt{\pi}$ (see Appendix)]. We may increase the saturation to $S_g=16\pi a^2$ in two different ways. In Figures 1b, a is constant, whereas in Figure 1c, b is constant.

When b is constant, we can deduce a critical water saturation, S_{wc}, for which the attenuation is maximum. For a given frequency, and using $S_w=1-(a/b)^3$, we obtain from equation (7):

$$S_{wc}=1-\left(1-\sqrt{\frac{\kappa K_{E2}}{\pi\eta_2 f b^2}}\right)^3. \tag{8}$$

If a is constant, the critical saturation is given by

$$S_{wc}=1-\left(1+\sqrt{\frac{\kappa K_{E2}}{\pi\eta_2 f a^2}}\right)^{-3}. \tag{9}$$

As stated in the Appendix, the size of the gas pockets, a, should be much smaller than the wavelength. Let us consider a reference velocity $c_r=3000$ m/s, a maximum outer radius $b=7$ mm, and $S_g=0.52$ [the upper-limit gas saturation for which White's model holds (see Appendix)]. Since $a=bS_g^{1/3}$, the condition $a\ll c_r/f$ implies $f\ll 536$ kHz. With these limitations in mind, we proceed in the following to analyze White's results and compare these results with numerical simulations.

The modeling algorithm uses a numerical mesh with rectangular cells (here we consider square cells). Let us assume that b is constant. Since the size of the elementary square $\ell=\sqrt{\pi}b=m\Delta x$, where m is a natural number and Δx is the grid spacing, $\Delta x=\sqrt{\pi}b/m$. If M is the number of cells of the gas pocket, then $M\Delta x^2=\pi a^2$, and $S_g=M/m^2$. On the other hand, if a is constant, the grid size is computed as $\Delta x=a\sqrt{\pi/M}$. An example of White's partial saturation model represented on a 2D numerical grid is shown in Figure 2, where water and gas are indicated by black and white colors, respectively. The model is an example for $a=2$ mm and a source central frequency of 100 kHz. The grid size is 208×208, and the grid spacing is $\Delta x=0.886$ mm (30 grid points are used for the absorbing boundaries at the sides of the mesh). A gas pocket is modeled with $M=16$ cells, $m=14$, $\ell=12.41$ mm, and $b=7$ mm. Water saturation is then $S_w=0.918$. The simulation corresponding to the model shown in Figure 2 uses a time step of 0.12 μs. The source in all the simulations is a Ricker wavelet applied to

Table 1. Material properties of the rock.

Grain	
Bulk modulus (K_s)	34.3 GPa
Shear modulus (μ_s)	35.3 GPa
Density (ρ_s)	2585 kg/m^3
Matrix	
Bulk modulus (K_m)	8.67 GPa
Shear modulus (μ_m)	6.61 GPa
Porosity (ϕ)	0.3
Permeability (κ)	0.55 d
Tortuosity ($\mathcal{T}$)	2.5
Gas	
Bulk modulus (K_g)	0.01 GPa
Density (ρ_g)	100 kg/m^3
Viscosity (η_g)	0.000 02 Pa s
Brine	
Bulk modulus (K_w)	2.4 GPa
Density (ρ_w)	1040 kg/m^3
Viscosity (η_w)	0.001 8 Pa s

the solid skeleton and the fluid phase (a bulk source without shear components). A region with a radius of 30 grid points and 100% water saturation surrounds the source location in order to obtain a uniform initial wavefront.

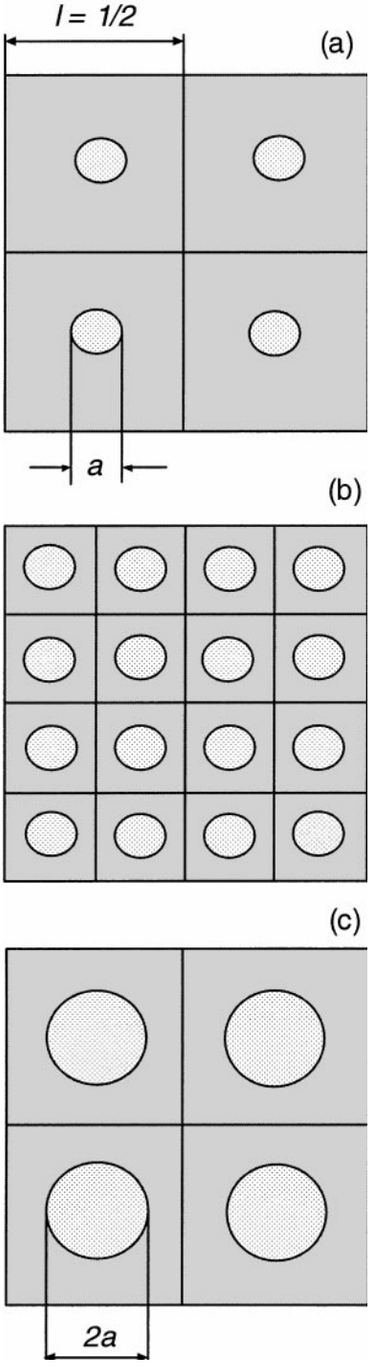

FIG. 1. Two different sizes for the gas pockets give the same gas saturation, depending on the values of the outer and inner radii a and b. In (a) the saturation is $S_g = 4\pi a^2$, whereas in (b) and (c) the saturation is the same and equal to four times the saturation in (a). Gas saturation can then change by varying a and keeping constant b, or vice versa. (Note that White considers an outer sphere of radius b instead of a cube of size ℓ. In 2D space, $b = \ell/\sqrt{\pi}$.)

Let us first consider that the radius of the outer sphere, b, is constant and equal to 4 mm. Figure 3 shows the P-wave velocity (a) and attenuation factor (b) versus water saturation for different frequencies and a permeability of 550 md. The analytical and numerical (black dots) evaluation of Gassmann's velocity has been performed on a homogeneous porous medium by averaging the fluid bulk modulus with Wood's equation (e.g., Mavko et al., 1998, 112). Gassmann's velocity (e.g. Carcione, 2001, 257) is also shown as a dotted curve. The critical water saturations, S_{wc}, for 50, 100, 250, and 500 kHz are 99%, 9%, 72%, and 56%, respectively (plus symbols). The differences in velocity can be important for increasing frequency. For instance, the difference between the seismic velocity (Gassmann's curve) and the ultrasonic velocity (100 kHz) predicted by White's model is 120 m/s at 90% water saturation [the respective wavelengths are approximately 150 m (seismic frequencies) and 3 cm (100 kHz)]. The simulations predict higher velocities compared to White's model, and the relaxation peaks are shifted towards lower water saturations. However, the physics revealed by the numerical results is similar to that predicted by White's model.

Figure 4 shows the P-wave velocity (a) and attenuation factor (b) versus water saturation for different permeabilities and a frequency of 100 kHz. The dotted line is Gassmann's velocity, obtained by mixing the fluid moduli with Wood's average. The critical water saturations, S_{wc}, for 0, 10, 100, 550, and 5000 md are 2%, 20%, 55%, 91% and 100%, respectively, in fairly good agreement with the location of the relaxation peaks predicted by White's model. The numerical phase velocities coincide with White's velocities for low permeabilities. For 550 and 5000 md, the simulations predict higher velocities. This means more velocity dispersion (see also the higher attenuation levels in

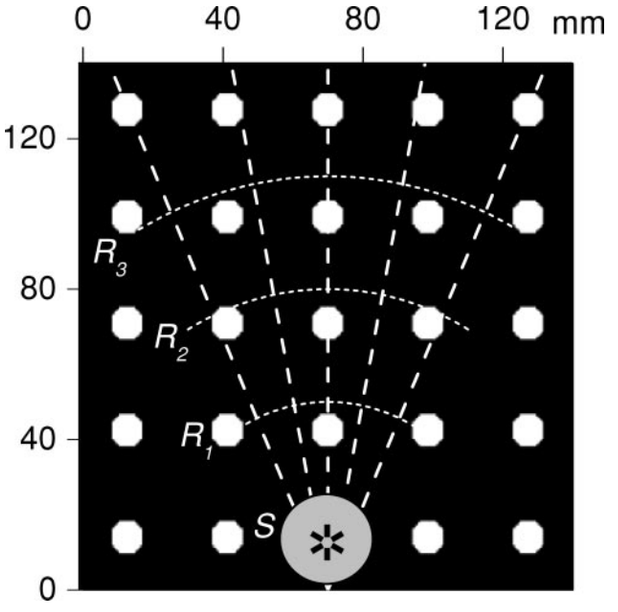

FIG. 2. White's model on a 2D numerical mesh used for wave simulation with a 100-kHz source. Water and gas are indicated by black and white colors, respectively. Source (S) and receivers (R_i) are indicated. A circular region surrounding the source is fully water saturated to assure a uniform initial wavefront. Gas pocket radius is $a = 2$ mm, and water saturation is $S_w = 0.918$ ($b = 7$ mm).

Figure 4b) caused by additional dissipation mechanisms which are not predicted by White's model.

Figure 5 shows the P-wave velocity (a) and attenuation factor (b) versus frequency for different water saturations. The permeability is 550 md. The critical frequencies, f_c, are indicated by plus symbols in Figure 5b. As before, higher velocities and attenuation levels, compared to White's model, are observed in the numerical simulations. The shift of the peaks towards lower frequencies can be an indication of the presence of local fluid flow mechanisms.

Let us assume now that the radius of the gas pockets, a, is constant and equal to 2 mm. The results, corresponding to Figures 3, 4, and 5, are respectively shown in Figures 6, 7, and 8. We observe the same physical behavior as for constant b, indicating that the physics is substantially dependent on the difference $b - a$.

Snapshots of the fluid particle velocity relative to the solid (a), fluid pressure (b), and particle velocity of the solid (c) are shown in Figure 9. They correspond to the model shown in Figure 2, with 92% water saturation but a central frequency of 500 kHz and a corresponding smaller grid spacing $\Delta x = 0.1$ mm in a 660×660 grid to highlight the details (54 grid points are used for the absorbing boundaries at the sides of the mesh). The two main wavefronts are the fast P-wave and the slow P-wave. The conversion of fast P-wave to slow P-wave at each gas pocket can clearly be appreciated. At 500 kHz, slow waves have a phase velocity of 841 m/s in the brine saturated region and 200 m/s in the gas pockets (the fast P-wave velocity is 3210 and 3094 m/s, respectively). The primary fast wave P^+ generates slow waves P^+P^- at the gas pockets. In addition, significant slow waves are generated by the scattered P^+ inside the gas pocket

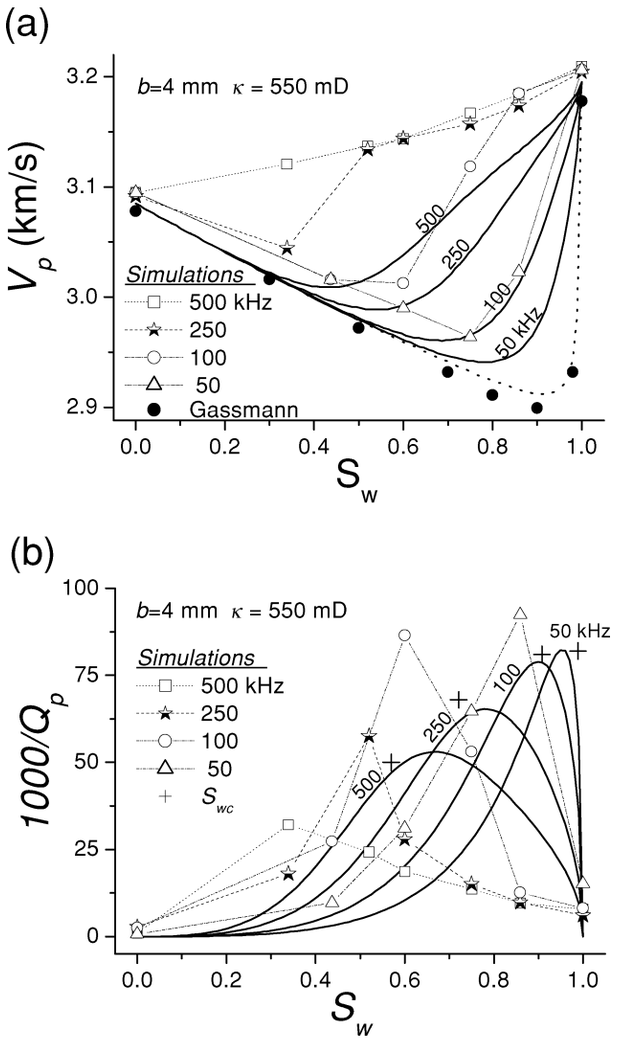

FIG. 3. P-wave velocity (a) and attenuation factor (b) versus water saturation for different frequencies and a permeability of 550 md. The continuous line corresponds to White's theory and the symbols to the numerical simulations. The dotted line is Gassmann's (low-frequency) velocity, obtained by mixing the fluid moduli with Wood's average. The size of the outer sphere is $b = 4$ mm.

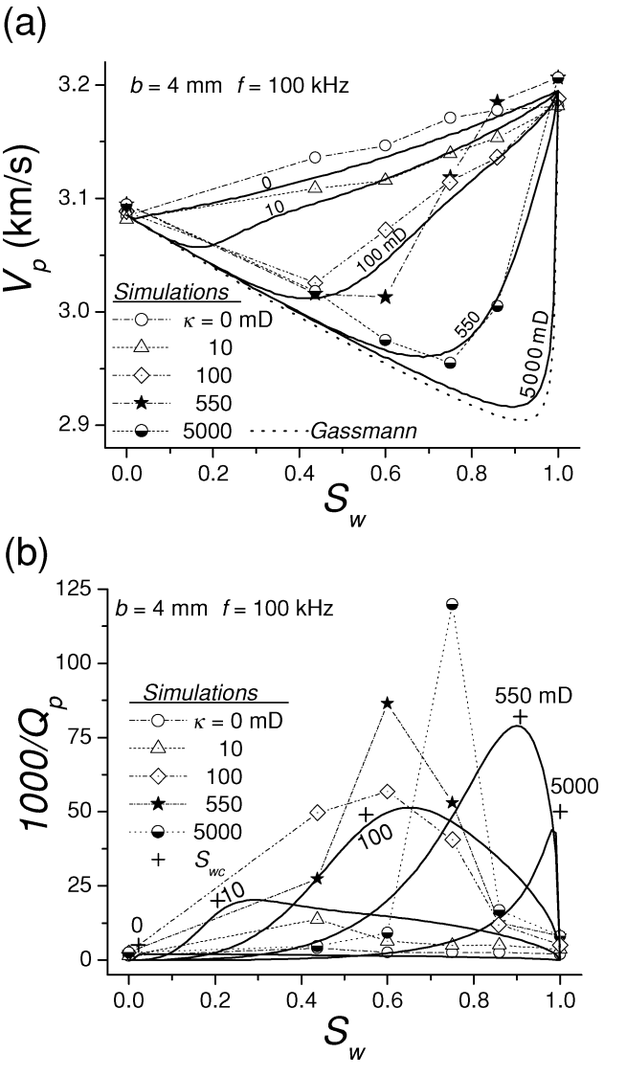

FIG. 4. P-wave velocity (a) and attenuation factor (b) versus water saturation for different permeabilities and a frequency of 100 kHz. The continuous line corresponds to White's theory and the symbols to the numerical simulations. The dotted line is Gassmann's (low-frequency) velocity, obtained by mixing the fluid moduli with Wood's average. The size of the outer sphere is $b = 4$ mm.

($P^+P^+P^-$). These are the two main events generated in the fluid phase during passage of the primary P^+, and thus represent the most significant loss components, removing energy from the front of the pulse and adding to its tail. The fluid particle velocity of the slow waves (Figure 9a) is high within the gas pocket and less pronounced in the brine, whereas for the fluid pressure (Figure 9b), the situation is the opposite. In the solid (Figure 9c), P^+ dominates the wavefield, while the slow waves are less clearly identified.

A final numerical experiment to illustrate the phenomenon is shown in Figure 10. Figure 10a shows a gas pocket of radius $a = 5$ mm with a circular source located at a distance $b = 23$ mm from its center. The rock and the pore fill are the same as in the previous experiment (Table 1). We use a fine mesh of $\Delta x = 0.1$ mm and a source frequency of 500 kHz. The seismograms of the particle velocity (Figure 10b) are recorded at receivers located 1 mm away from the fluid/gas boundary in the water-saturated and gas-saturated rocks. In the solid, it shows the P^+ arrival and its scattering $P_C P^+$ with opposite phase after focusing in the center of the gas pocket. In the fluid wavefield, we observe the corresponding slow waves $P_B P^-$ and $P_C P^-$, generated at the the fluid/gas boundary. These are equivalent to the two consecutive slow waves apparent from the experiment in Figure 9. The tail of arrivals recorded within the gas zone, following the main events, are slow waves due to P^+ ringing within the gas pocket, whereas the late P^- events at the end of the record are the direct (in the brine) and transmitted (in the gas) slow wave generated at the source.

More details of these experiments can be appreciated in Figure 11, which shows the seismograms of the fluid (relative) (a) and solid (b) particle velocities along the receiver line. The fast- and slow-wave events are clearly distinguishable by their different dips [i.e., low angles (high velocity) for P^+ and high angles (low velocity) for P^-]. The focusing of the direct P^+ is well expressed in both fluid and solid particle velocities, and a similar focusing of P^+ is evident in the lower section of (b), originating from P^- to P^+ conversion at the water/gas interface. The latter, however, has less relevance for the problem at hand

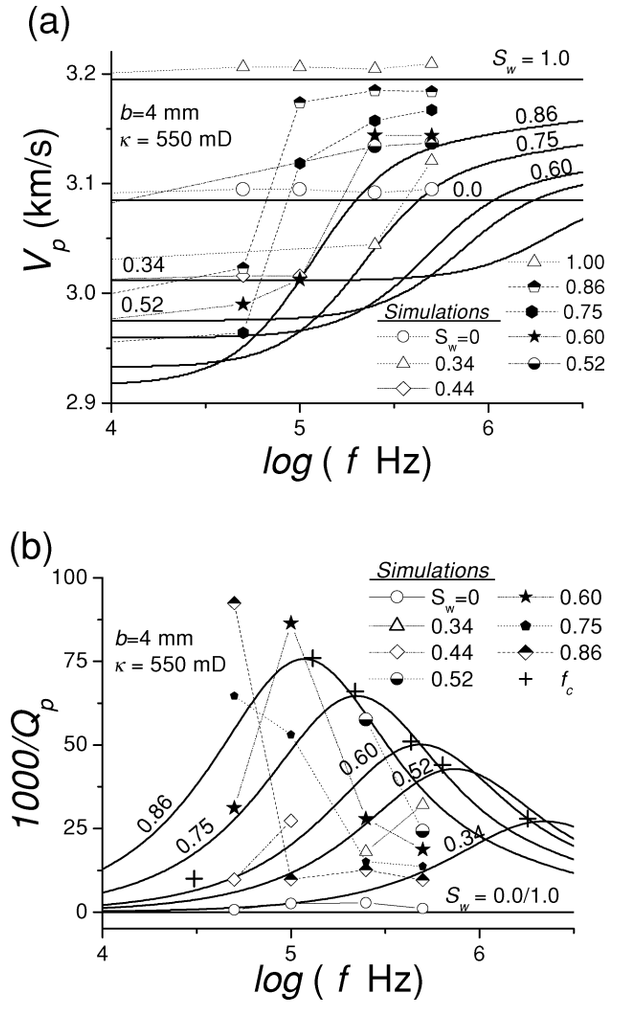

FIG. 5. P-wave velocity (a) and attenuation factor (b) versus frequency for different water saturations. The continuous line corresponds to White's theory and the symbols to the numerical simulations. The permeability is 550 md. The size of the outer sphere is $b = 4$ mm. The location of critical frequencies is indicated for different saturations.

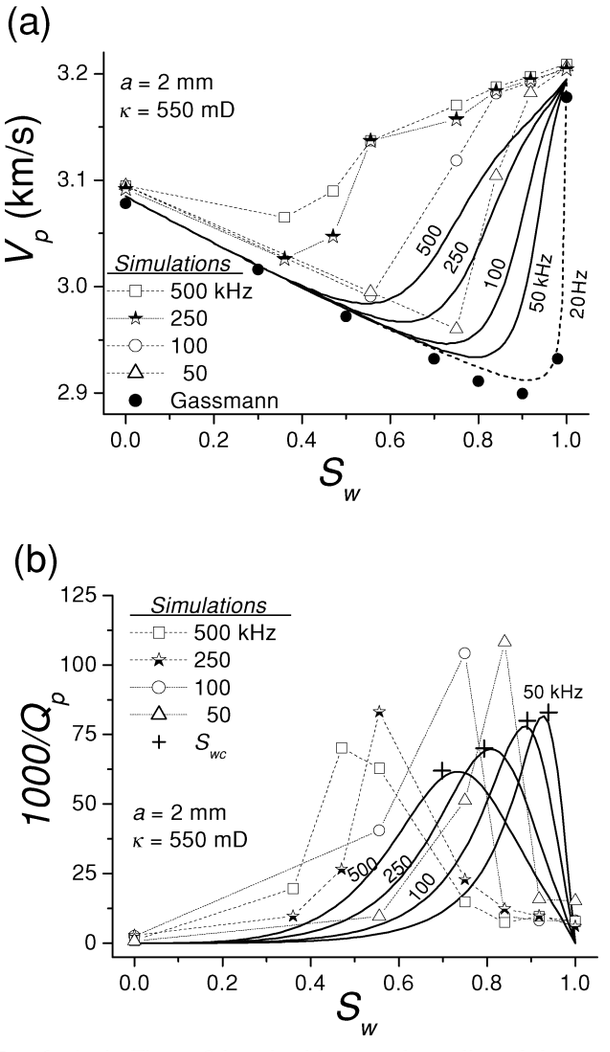

FIG. 6. As in Figure 3 but, in this case, the radius of the gas pockets is $a = 2$ mm.

since this event is confined to the tail of the recorded pulse. On the other hand, the first event is important since it interferes with the primary pulse and, moreover, continues to bounce around within the gas pocket (b) generating multiples of slow waves propagating inwards in the gas zone as well as outwards in the fluid zone (a). The two most significant slow-wave events, as shown in Figure 10a (P_BP^- and P_CP^-) are clearly separated in both seismograms.

CONCLUSIONS

Fast P-wave conversion into slow P-waves (mostly) and S-waves is the main mechanism of wave dissipation and velocity dispersion in partially saturated rocks. This phenomenon is observed in our numerical simulations, and is partially predicted by White's (1975) model, regarding the slow P-wave motion. Norris (1993) and Gurevich and Lopatnikov (1995), using alternating poroelastic layers, have shown that attenuation and velocity dispersion measurements can be explained by the combined effect of layering and energy transfer between wave modes. If the fluid compressibility varies significantly from point to point, diffusion of pore fluid between different regions constitutes a mechanism that can be important at seismic frequencies. Carcione (1998) observed this strong dissipation in numerical simulations of wave propagation in alternating plane layers saturated with water and gas. This phenomenon may explain the low signal-to-noise P-wave sections observed in some ocean-bottom seismic data (Kommedal et al., 1997). In fact, the presence of gas, leaked from the reservoir to the overburden, has the effect of both lowering seismic velocities and increasing seismic attenuation, producing low signal-to-noise ratio P-wave sections (this effect is not present in S-wave sections).

In general, our simulations predict higher attenuation (although narrower relaxation peaks) and higher velocities than White's model. This is due to additional wave dissipation due to multiple scattering and wave conversion. Moreover, White's model does not take into account local fluid flow effects (Gist, 1994), whereas they are present in the numerical simulations (these effects increase the velocity). Another source of discrepancy between model and numerical experiments can be attributed to the fact that the grid representations of the gas pockets are not exactly circles because the mesh is composed of rectangular cells. We obtain expressions of the relaxation

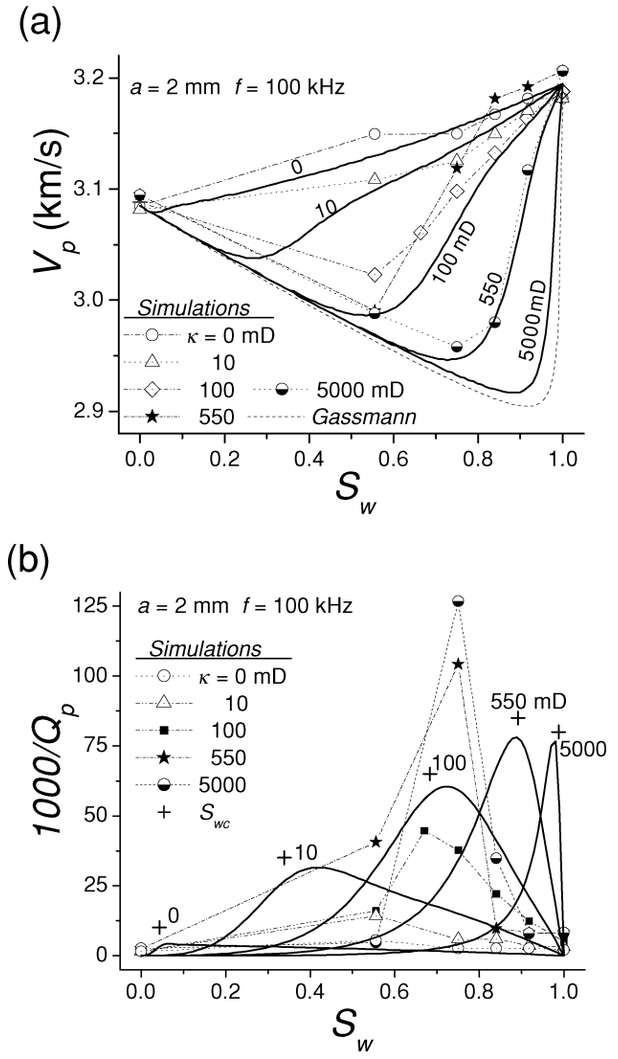

FIG. 7. As in Figure 4 but, in this case, the radius of the gas pockets is $a = 2$ mm.

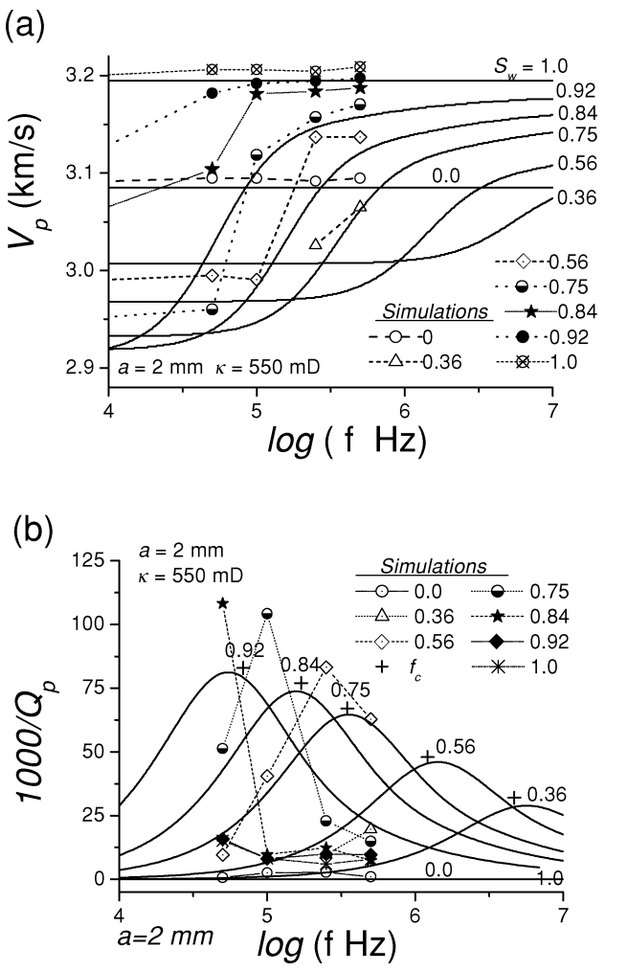

FIG. 8. As in Figure 5 but, in this case, the radius of the gas pockets is $a = 2$ mm.

critical frequency and critical saturation for which attenuation has a maximum value. Our simulations reproduce the trends regarding the location of the relaxation peaks as a function of frequency and saturation. That is, the peaks move towards higher water saturations for lower frequencies and higher permeabilities.

The final example shows an analysis of the wavefield for a single gas pocket, modeling the conditions for which White (1975) has developed the theory. The physical phenomena involved in the problem are illustrated by this simulation. The conversion from fast to slow compressional wave and the multiple events generated at the gas bubble are clearly the main loss mechanisms of the primary pulse.

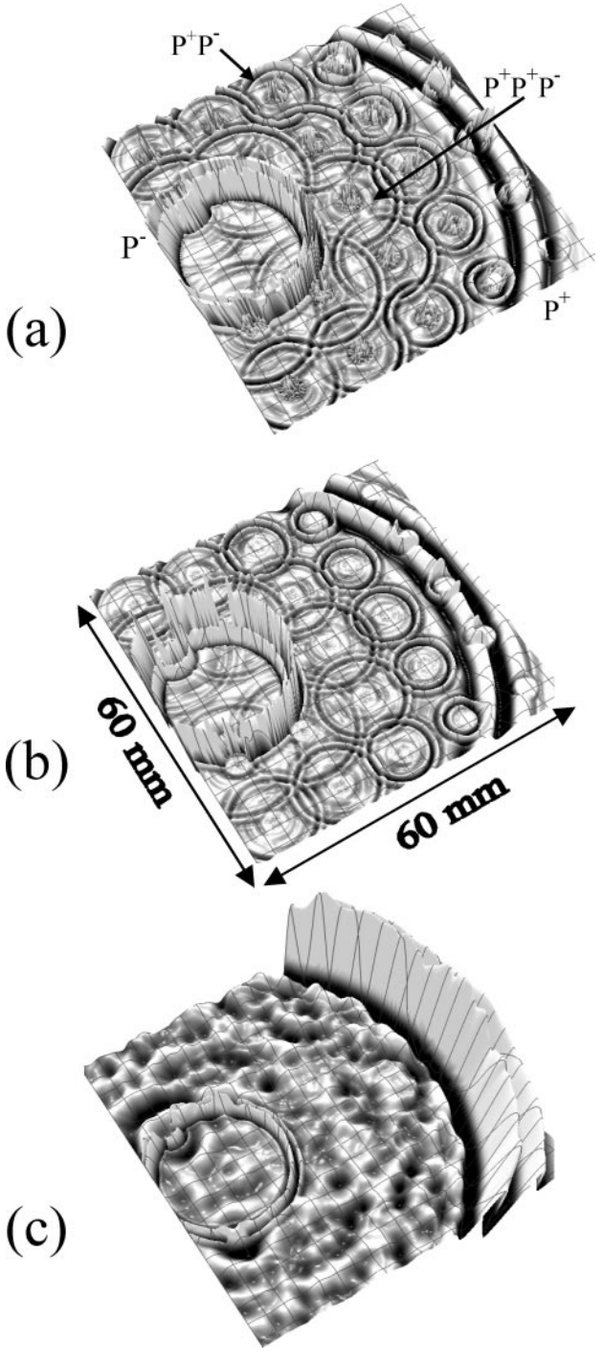

FIG. 9. Snapshot of the fluid particle velocity relative to the solid (a), fluid pressure field (b), and particle velocity of the solid (c), corresponding to the model shown in Figure 2 with 92% water saturation but with finer mesh (0.1 mm) and a central frequency of 500 kHz. Propagation time is 18 μs. The primary fast P^+ wave generates slow waves (P^+P^-) at the gas pockets. Fast waves scattered from the inner boundary, in turn, generate new slow waves ($P^+P^+P^-$).

ACKNOWLEDGMENTS

This work was financed in part by the European Union under the HYGEIA project and by the Norwegian Research Council under the PetroForsk programme (N. H. Pham). We

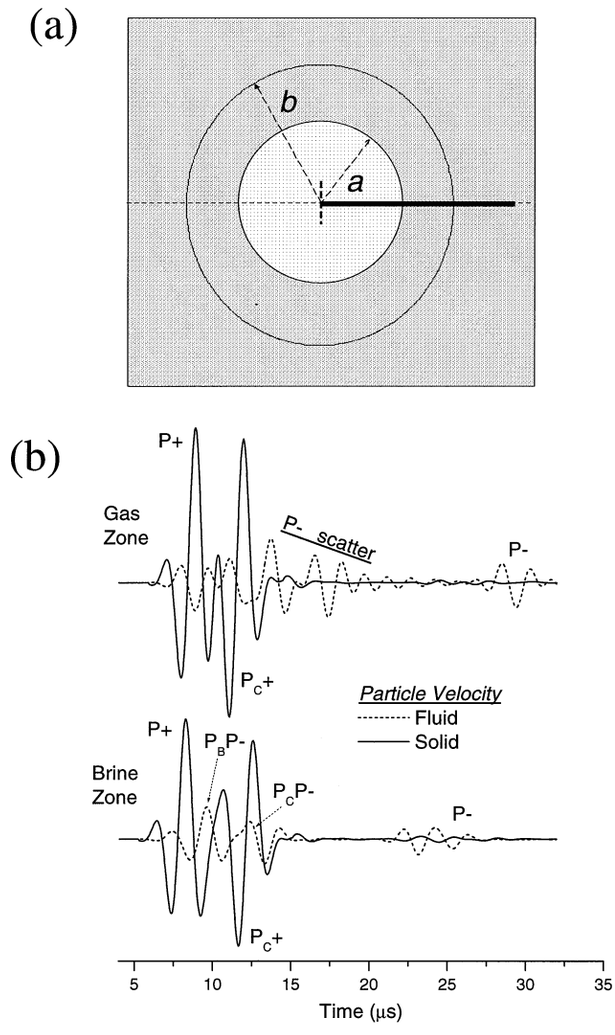

FIG. 10. Model of a single gas pocket of radius $a = 5$ mm and a circular source located at a distance $b = 23$ mm (a). Fluid (relative) and solid particle velocities (b) are recorded in receivers located on either side (1 mm) of the gas/fluid boundary. The solid line indicates receivers for the seismograms in Figure 11. P^+ denotes the direct fast wave and $P_C P^+$ its return from the pocket center (focus). $P_B P^-$ and $P_C P^-$ are their associated slow waves generated at the intersection with the gas/fluid boundary. The central frequency is 500 kHz, the grid size is 0.1 mm, and time step is 0.013 22 ms.

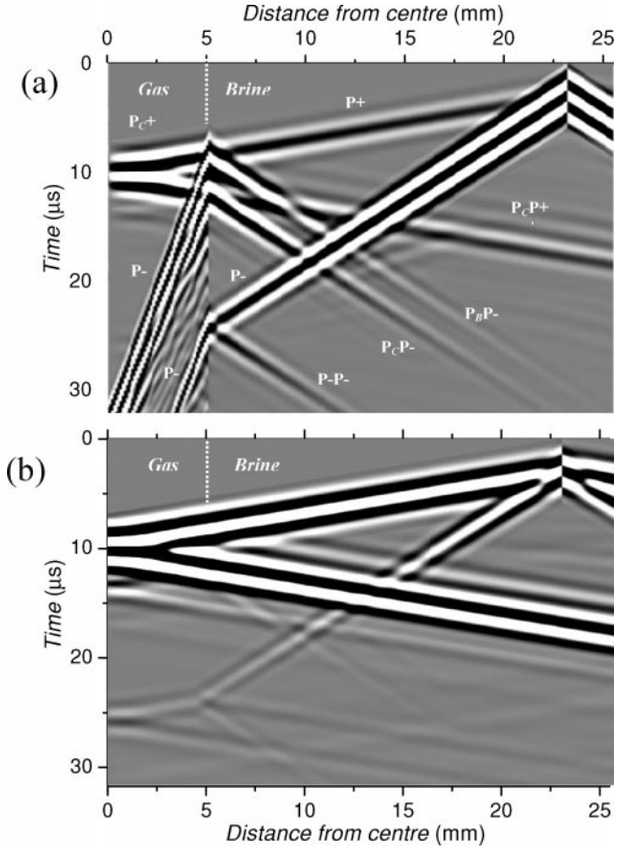

FIG. 11. Seismograms of the fluid particle velocity relative to the solid (a) and particle velocity of the solid (b), corresponding to the model shown in Figure 10. Note the slow wave generation at the gas/water boundary by the primary P^+ and their multiple events generated within the gas pocket. The two slow waves P_BP^- and P_CP^- shown in Figure 10 can clearly be seen.

thank Boris Gurevich and an anonymous reviewer for useful suggestions.

REFERENCES

Cadoret, T., Marion, D., and Zinszner, B., 1995, Influence of frequency and fluid distribution on elastic wave velocities in partially saturated limestones: J. Geophys. Res., **100**, 9789–9803.
Carcione, J. M., 1996, Wave propagation in anisotropic, saturated porous media: Plane wave theory and numerical simulation: J. Acoust. Soc. Am., **99**, 2655–2666.
——— 1998, Viscoelastic effective rheologies for modeling wave propagation in porous media: Geophys. Prosp., **46**, 249–270.
——— J. M., 2001, Wave fields in real media: Wave propagation in anisotropic, anelastic and porous media: Pergamon Press Inc.
Carcione, J. M., Gurevich, B., and Cavallini, F., 2000, A generalized Biot-Gassmann model for the acoustic properties of clayley sandstones: Geophys. Prosp., **48**, 539–557.
Carcione, J. M., and Helle, H. B., 1999, Numerical solution of the poroviscoelastic wave equation on a staggered mesh: J. Comput. Phys., **154**, 520–527.
Carcione, J. M., and Quiroga-Goode, G., 1996, Full frequency range transient solution for compressional waves in a fluid-saturated viscoelastic porous medium: Geophys. Prosp., **44**, 99–129.
Carcione, J. M., Quiroga-Goode, G., and Cavallini, F., 1996, Wavefronts in dissipative anisotropic media: Comparison of the plane wave theory with numerical modeling: Geophysics, **61**, 857–861,
Dutta, N. C., and Odé, H., 1979, Attenuation and dispersion of compressional waves in fluid-filled porous rocks with partial gas saturation (White model)—Part II: Results: Geophysics, **44**, 1789–1805.
Dutta, N. C., and Seriff, A. J., 1979, On White's model of attenuation in rocks with partial saturation: Geophysics, **44**, 1806–1812.
Gist, G. A., 1994, Interpreting laboratory velocity measurements in partially gas-saturated rocks, Geophysics: **59**, 1100–1109.
Goldberg, I., and Gurevich, B., 1998, A semi-empirical velocity-porosity-clay model for petrophysical interpretation of P- and S-velocities: Geophys. Prosp., **46**, 271–285.
Gurevich, B., and Lopatnikov, S. L., 1995, Velocity and attenuation of elastic waves in finely layered porous rocks: Geophys. J. Internat, **121**, 933–947.
Johnson, D. L., 2001, Theory of frequency dependent acoustics in patchy-saturated porous media: J. Acoust. Soc. Am., **110**, 682–694.
Johnson, D. L., Koplik, J., and Dashen, R., 1987, Theory of dynamic permeability and tortuosity in fluid-saturated porous media: J. Fluid Mech., **176**, 379–402.
Knight, R., and Nolen-Hoecksema, R., 1990, A laboratory study of the dependence of elastic wave velocities on pore scale fluid distribution: Geophys. Res. Lett., **17**, 1529–1532.
Kommedal, J. H., Barkved, O. I., and Thomsen, L., 1997, Acquisition of 4 component OBS data—A case study from the Valhall field: 59th Ann. Internat. Mtg., Eur. Assoc. Expl. Geophys., Expanded Abstracts, B047.
Krief, M., Garat, J., Stellingwerff, J., and Ventre, J., 1990, A petrophysical interpretation using the velocities of P and S waves (full waveform sonic): The Log Analyst, **31**, 355–369.
Mavko, G., Mukerji, T., and Dvorkin, J., 1998, The rock physics handbook: Tools for seismic analysis in porous media: Cambridge Univ. Press.
Murphy, W. F., III, 1984, Acoustic measures of partial gas saturation in tight sandstones, J. Geophys. Res., **89**, B13, 11549–11559.
Norris, A. N., 1993, Low-frequency dispersion and attenuation in partially saturated rocks: J. Acoust. Soc. Am., **94**, 359–370.
Toksöz, N. N., Johnston, D. H., and Timur, A., 1979, Attenuation of seismic waves in dry sand saturated rocks: I. Laboratory measurements: Geophysics, **44**, 681–690.
White, J. E., 1975, Computed seismic speeds and attenuation in rocks with partial gas saturation: Geophysics, **40**, 224–232.
White, J. E., Mikhaylova, N. G., and Lyakhovitsky, F. M., 1975, Low-frequency seismic waves in fluid saturated layered rocks: Izvestija Acad. Sci. USSR, Phys. Solid Earth, **11**, 654–659.
Winkler, K. W., and Nur, A., 1982, Seismic attenuation: Effects of pore fluid and frictional sliding: Geophysics, **47**, 1–15.
Yin, C. -S., Batzle, M. L., and Smith, B. J., 1992, Effects of partial liquid/gas saturation on extensional wave attenuation in Berea sandstone: Geophys. Res. Lett., **19**, 1399–1402.

APPENDIX A

WHITE'S MODEL FOR PARTIAL SATURATION

White (1975) assumed spherical gas pockets much larger than the grains but much smaller than the wavelength. He developed the theory for a gas-filled sphere of porous medium of radius a located inside a water-filled cube of porous medium. For simplicity in the calculations, White considers an outer sphere of radius b ($b > a$), instead of a cube. Thus, the system consists of two concentric spheres, where the volume of the outer sphere is the same as the volume of the original cube. In 3D space, the outer radius is $b = \ell/(4\pi/3)^{1/3}$, where ℓ is the size of the cube. In 2D space, the outer radius is $b = \ell/\sqrt{\pi}$, where ℓ is the size of the square. The distance between pockets is ℓ. Let us denote the saturation of gas and water (brine) by $S_1(S_g)$ and $S_2(S_w)$, respectively, such that $S_1 + S_2 = 1$. Then $S_1 = a^3/b^3$ in 3D space and $S_1 = a^2/b^2$ in 2D space. When $a = \ell/2$, the gas pockets touch each other. This happens when $S_1 = \pi/6 = 0.52$ in 3D space. Therefore, for values of the gas saturation higher than these critical value, or values of the water saturation between 0 and 0.48, the theory is not rigorously valid. Another limitation to consider is that the size of gas pockets should be much smaller than the wavelength (i.e., $a \ll c_r/f$, where c_r is a reference velocity and f is the frequency).

The complex P-wave velocity is given by

$$v_c = \sqrt{\frac{K + 4\mu_m/3}{\rho}}, \tag{A-1}$$

where K is the complex bulk modulus (given below), μ_m is the dry-rock shear modulus, and ρ is the effective density.

The dry-rock moduli K_m and μ_m can be obtained, for instance, from laboratory measurements in dry samples. If c_P and c_S are the experimental dry-rock compressional and shear velocities, the moduli are approximately given by

$$K_m = (1-\phi)\rho_s\left(c_P^2 - \frac{4}{3}c_S^2\right), \quad \mu_m = (1-\phi)\rho_s c_S^2, \tag{A-2}$$

where ρ_s is the grain density and ϕ is the porosity.

The effective density is given by

$$\rho = (1-\phi)\rho_s + \phi\rho_f, \tag{A-3}$$

where

$$\rho_f = S_1\rho_{f1} + (1-S_1)\rho_{f2}, \tag{A-4}$$

and ρ_{f1} and ρ_{f2} are the densities of fluid 1 and fluid 2 (gas and water in White's theory).

Assuming that the dry-rock and grain moduli, and permeability, κ, of the different regions are the same, the complex bulk modulus as a function of frequency is given by

$$K = \frac{K_\infty}{1 - K_\infty W}, \tag{A-5}$$

where

$$\begin{aligned}
W &= \frac{3ia\kappa(R_1 - R_2)}{b^3\omega(\eta_1 Z_1 - \eta_2 Z_2)}\left(\frac{K_{A1}}{K_1} - \frac{K_{A2}}{K_2}\right),\\
R_1 &= \frac{(K_1 - K_m)(3K_2 + 4\mu_m)}{K_2(3K_1 + 4\mu_m) + 4\mu_m(K_1 - K_2)S_1},\\
R_2 &= \frac{(K_2 - K_m)(3K_1 + 4\mu_m)}{K_2(3K_1 + 4\mu_m) + 4\mu_m(K_1 - K_2)S_1},\\
Z_1 &= \frac{1 - \exp(-2\gamma_1 a)}{(\gamma_1 a - 1) + (\gamma_1 a + 1)\exp(-2\gamma_1 a)},\\
Z_2 &= \\
&\frac{(\gamma_2 b + 1) + (\gamma_2 b - 1)\exp[2\gamma_2(b-a)]}{(\gamma_2 b + 1)(\gamma_2 a - 1) - (\gamma_2 b - 1)(\gamma_2 a + 1)\exp[2\gamma_2(b-a)]},
\end{aligned} \tag{A-6}$$

$$\begin{aligned}
\gamma_j &= \sqrt{i\omega\eta_j/(\kappa K_{Ej})},\\
K_{Ej} &= \left[1 - \frac{\alpha K_{fj}(1 - K_j/K_s)}{\phi K_j(1 - K_{fj}/K_s)}\right]K_{Aj},\\
K_{Aj} &= \left[\frac{\phi}{K_{fj}} + \frac{1}{K_s}(\alpha - \phi)\right]^{-1},\\
\alpha &= 1 - \frac{K_m}{K_s}.
\end{aligned}$$

$$K_\infty = \frac{K_2(3K_1 + 4\mu_m) + 4\mu_m(K_1 - K_2)S_1}{(3K_1 + 4\mu_m) - 3(K_1 - K_2)S_1} \tag{A-7}$$

is the (high-frequency) bulk modulus when there is no fluid flow between the gas pockets. K_1 and K_2 are the (low-frequency) Gassmann moduli, which are given by

$$K_j = \frac{K_s - K_m + \phi K_m\left(K_s/K_{fj} - 1\right)}{1 - \phi - K_m/K_s + \phi K_s/K_{fj}}, \quad j = 1, 2. \tag{A-8}$$